JACS
JOURNAL OF THE AMERICAN CHEMICAL SOCIETY
Article
Cite This: *J. Am. Chem. Soc.* 2019, 141, 5241−5251
pubs.acs.org/JACS

Electronic Excitation Dynamics in DNA under Proton and α-Particle Irradiation

Dillon C. Yost and Yosuke Kanai*

Department of Chemistry, The University of North Carolina at Chapel Hill, Chapel Hill, North Carolina 27599, United States

Supporting Information

ABSTRACT: Electronic excitations are produced when matter is exposed to ion irradiation comprising highly energetic ions. These electronic stopping excitations are responsible for ion beam-induced DNA damage by energetic protons and α-particles, the chemistry and physics of which are central to burgeoning radiation cancer therapies. By simulating the non-perturbative electronic response of DNA to irradiating protons and α-particles, our first-principles dynamics simulations enable us to test the validity of the commonly used linear response theory description, and they also reveal unprecedented details of the quantum dynamics of electronic excitations. In this work, we discuss the extent to which the linear response theory is valid by comparing to the first-principles determination of electronic stopping power, the energy-transfer rate from ions to electronic excitation. The simulations show that electronic excitations induced by proton and α-particle irradiation cause ionization of DNA, resulting in the generation of holes. By studying the excited hole generation in terms of both the energetic and spatial details in DNA, our work reveals remarkable differences with the excitation behavior of DNA under more commonly used ionizing irradiation sources such as X/γ-ray photons. Furthermore, we find that the generation of excited holes does not directly correlate with the energy-transfer rate as a function of the irradiating ion velocity, in contrast to what is often assumed in the chemistry and physics of radiation oncology.

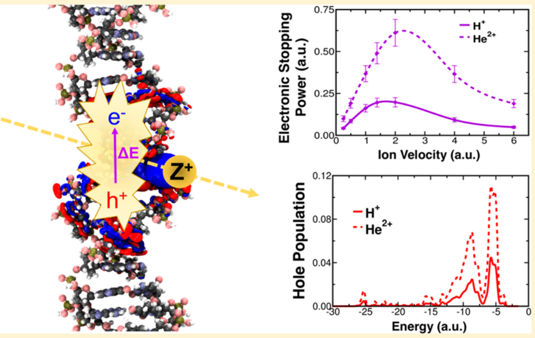

1. INTRODUCTION

When an irradiating ion penetrates matter, it transfers its kinetic energy via collisions with both the nuclei and the electrons in the material. For irradiating ions with high kinetic energies (> ∼10 keV/nucleon), the ion's kinetic energy can be rapidly transferred via inelastic collisions to electrons in the target material. This phenomenon, known as electronic stopping, has garnered much attention in the scientific community in recent years partly due to the increasing interest in ion beam cancer therapy.[1−3] Fast-moving ions such as protons, α-particles, and carbon ions have shown clinical promise in radiation oncology due to their distinctive energy dose-depth distributions.[4,5] Unlike high-energy photons such as X/γ-rays, irradiative ions deposit the vast majority of their energy at the end of their penetration range.[6,7] In principle, this allows for more precise targeting of tumor sites and increased preservation of surrounding healthy tissue.[8] The depth-dependent energy deposition profile of ions derives from the electronic stopping power, a quantity which describes the energy-transfer rate per unit length of the ion movement, which is a function of the projectile ion velocity.

In addition to determining the electronic stopping power accurately in biologically relevant materials (water, DNA, etc.), deciphering the physical and chemical mechanisms for how the energy deposition leads to DNA damage is a pressing challenge of paramount importance in ion-beam cancer therapy. Generally, DNA radiation damage is discussed in the context of direct and indirect effects. Direct effects comprise processes in which the DNA molecule itself is directly excited and/or ionized by the radiation, leading to critical bond breaking of the nucleobase pairs or more severe sugar-phosphate side chain damage such as double-strand breaks (DSBs).[9,10] Indirect effects comprise events in which radiation induces secondary electron generation and/or creation of reactive species (e.g., water radiolysis products like OH radicals), which can then proceed to chemically react with the DNA molecule, inducing damage.[11,12] The common view is that DSBs and/or clustering of DSBs play a key role in cell death.

While much progress has been made in deciphering DNA damage mechanisms under various types of irradiation, significant ambiguities and controversies remain. For example, a recent work by Nguyen et al. on DNA damage under UV irradiation indicates that secondary electrons have greater significance in DNA damage than OH radicals,[13,14] contrary to the conventional view developed with low-energy electron radiation.[15,16] For ionizing radiation like X/γ-rays, both direct and indirect effects can be operative, and some have reported significantly higher DSB yields in the presence of water under γ-ray radiation.[17]

For protons and other types of ion radiation, often referred to as densely ionizing radiation, the direct effect is generally

Received: November 12, 2018
Published: March 13, 2019

ACS Publications

DOI: 10.1021/jacs.8b12148

assumed to play a more prominent role in DSB formation because much more energy can be deposited in a small region around DNA.[18] Despite this well-reasoned assumption, there lacks a firm consensus as to the relative importance of direct effects versus indirect effects for ion irradiation in the existing literature.[16] Although proton (and heavier ion) radiation is classified under the same term "ionizing radiation" just like X/γ-ray radiation, the modern scientific understanding of particle radiation in this regard is still quite limited. With direct effects of particle radiation, the details are murky at best, partly because the process is highly complex and multiscale in nature: It involves atto/femtosecond dynamics of electronic excitation, femto/picosecond dynamics of excited hole relaxation, and chemical reactions that occur on much longer time scales. The physics that govern the entire process range from quantum-mechanical excitations of electrons in the initial DNA irradiation all the way to microscopic biochemical changes that are responsible for cell death.

In modern proton beam cancer therapy, proton beams are calibrated for radiation oncology treatment by adapting the so-called relative biological effectiveness (RBE) with respect to a photon (i.e., X-rays, γ-rays) standard.[19,20] A fundamental assumption here is that the relevant DNA damage formation mechanism is the same under proton irradiation as the more widely studied X/γ-ray irradiation. However, various studies find that this empirically determined RBE depends on various factors including radiation dose and the stopping power itself. Researchers such as Loeffler and Durante have called for more detailed investigation so that mechanistic understanding beyond the RBE notion can be obtained.[21]

Increasing numbers of studies are now aimed at developing scientific bases that incorporate molecular-scale details in order to understand and model ion beam therapies,[22−24] including very recent work combining both experimental and simulation methods to understand the damage mechanisms of α-particle irradiated molecular systems.[25] Also notably, recent work by Souici et al.[26] studied how different DNA damage and fragmentation depends on the electronic stopping power (i.e., linear energy transfer (LET) as often called in oncology) and the dose of proton radiation. Although DNA is solvated by water in physiological conditions, most spectroscopic measurements under irradiation are performed on dry DNA to allow for detailed characterization,[27,28] like in the work by Souici et al.[26] Using the SRIM model for electronic stopping power, Souici et al.[26] reported that damage such as single-strand breaks (SSBs) and DSBs indeed depend significantly on the kinetic energy of the proton. It is often assumed that the velocity of maximum LET, the Bragg peak, gives rise to the most damage. However, Souici et al. observed that the maximum response in terms of the damage was not observed for the Bragg peak proton velocity (of the popular SRIM model)[29] but rather for velocities beyond the Bragg peak (thus lower electronic stopping power). Furthermore, comparison of their work to an earlier study using α-particles shows that proton and α-particle beams result in different DNA damage yields, even for the velocities that give the same stopping power.[30]

These interesting observations call for studies into how electronic excitation, particularly ionization, is linked with electronic stopping power. Additionally, the SRIM electronic stopping power model[29] also comes with considerable uncertainties for biomolecular systems like DNA, and further advances on the electronic stopping power calculation itself are desired. In this regard, Abril et al. have recently reported the so-called MELF-GOS method based on model dielectric function fitted to experimental optical measurement,[31] and it is of great interest to also develop a quantum-mechanical description of the stopping power from first-principles calculations.

Although quantum-mechanical computational approaches such as first-principles molecular dynamics (FPMD)[32] based on density functional theory (DFT) have been used to study molecular processes in the context of DNA damage, most studies so far have focused on atomistic changes *after* the irradiation. With the rise of peta-scale supercomputers and the oncoming advent of exa-scale supercomputers,[33] in conjunction with the development of efficient massively parallel first-principles electron dynamics codes,[34−38] it has now become possible to directly simulate electronic excitation dynamics in ion irradiation for complex macromolecules like DNA without the need for any empirical parameters. In particular, real-time time-dependent density functional theory (RT-TDDFT) simulations provide a promising avenue to study the non-perturbative electronic response of DNA under ion irradiation with atomistic levels of detail. This approach has been recently employed to study the electronic stopping of liquid water under proton and α-particle irradiation[39,40] as well as in other materials. In this work, we report a RT-TDDFT-based, first-principles study of the electronic stopping process in DNA under proton and α-particle irradiation.

2. THEORY AND COMPUTATIONAL METHOD

The first-principles method based on RT-TDDFT we employ in this work closely follows that described by Schleife et al.[34,41] The time integration of the electronic states is performed using an enforced time reversal symmetry (ETRS) algorithm.[42] In this work, we use the Qb@ll branch of the Qbox code,[43] in which we implemented a highly scalable, massively parallel RT-TDDFT scheme based on the plane-wave pseudopotential formalism. Details of this code can be found in the work by Schleife et al.[34,41] and Draeger et al.[35] We use RT-TDDFT for obtaining the non-pertubative electronic response of a target material to a swift ionizing charged particle. In this work, the target material is a strand of neutral B-DNA in vacuum. The "dry" DNA molecule is a logical starting point for theoretical studies due to its relative simplicity and importantly also because most experimental/spectroscopic measurements are performed on dry DNA.[26−28,44] The planewave RT-TDDFT implementation involves simulation cells with periodic boundary conditions. The DNA in the simulation cell comprises 10 base pairs (CGCGCTTAAG sequence), one full turn of the double helix, ensuring that the periodic images in the z direction are commensurate with the periodicity of the macromolecule. A cubic simulation cell with dimensions of 34.43 Å was used, giving the appropriate length of the target strand and at the same time being wide enough in the x and y directions to avoid self-interactions neighboring periodic image. In total, the molecular system comprises 654 atoms (2220 electrons), which are represented by norm-conversing Hamann−Schluter−Chiang−Vanderbilt (HSCV) pseudopotentials.[45,46] This conventional pseudopotential approach is unable to model the potential "shake-up" effects[47] caused by core electrons, but such effects would have a negligible contribution in the results presented here.[48] The projectile ions, protons and α-particles, are treated on the same footing as the atoms in the DNA molecule, by HSCV pseudopoten-

DOI: 10.1021/jacs.8b12148
J. Am. Chem. Soc. 2019, 141, 5241−5251

tials. In their respective initial states, the proton and α-particle are fully ionized (H^+ and He^{2+}). At the beginning of each simulation, the initial position and velocity vector of the ion is specified, and at each time step, the position of the ion is updated based on its velocity, which is held constant. The time-dependent Kohn−Sham (TDKS) equations are integrated for this system in which the classical, energetic proton or α-particle travels through the simulation cell containing the DNA strand, giving rise to a time-dependent external potential acting on the electronic system of the molecule. While the position of the projectile ion changes and the electron density is updated, the atoms of the DNA molecule are held fixed. The time scales of the RT-TDDFT simulations (ranging from 0.26 to 6.3 fs, depending on the ion velocity) are too short for any appreciable nuclear motion in the DNA, making this frozen target atom approximation appropriate for studying the excitation dynamics as investigated in this work. We note, however, that subsequent processes such as intermolecular Coulombic decay[25] and hole relaxation[49,50] occur on longer time scales, in which cases it is essential to include nuclear motion. All simulations use a time step of 2.0 attoseconds. A planewave cutoff energy of 50 Ry was used. For the exchange−correlation (XC) approximation, we used the non-empirical PBE generalized gradient approximation (GGA) functional,[51] due its balance between accuracy and efficiency. GGA functionals such as PBE could exhibit artificial charge delocalization in certain cases.[52] However, previous RT-TDDFT studies comparing the PBE functional with hybrid XC functionals such as PBE0[53] and LC-BLYP[54] for the calculation of electronic stopping power[39,55] and projectile ion effective charge[39] show good quantitative agreement between GGAs and hybrids. As in most RT-TDDFT studies, we employ the adiabatic approximation for the XC functional's time dependence, resulting in an XC potential that depends only on the instantaneous electron density, neglecting any memory effects.[56] Going beyond the adiabatic approximation is an active area of research, especially in the context of RT-TDDFT,[57−59] but it is beyond the scope of this work. The adiabatic XC approximation in the context of RT-TDDFT calculations for electronic stopping power has been discussed in more detail in our earlier technical work.[55]

Figure 1 shows snapshots of a representative RT-TDDFT simulation performed in this work, with isosurfaces showing the electronic response to a proton penetrating through the DNA molecule. At time $t = 0$ au, the DNA remains in its ground state, thus, no induced densities are observed. But as the ion moves through the DNA molecule, there are fluctuations in the time-dependent electron density relative to the ground state, which is caused by the moving potential of the proton. While RT-TDDFT simulations are becoming more widely used, simulations at this scale (2220 electrons) are anything but routine. Using the aforementioned scalable Qb@ll code, the simulations in this study were performed using between 8192 and 131,072 IBM BG/Q cores on the Mira supercomputer at the Argonne Leadership Computing Facility. Without these petascale computational capabilities, such a study would not be possible.

3. RESULTS AND DISCUSSION

We organize the discussion of our quantum dynamics simulation results as follows. First, we discuss the calculation of electronic stopping power, which represents the rate of energy transfer as a function of the ion velocity. We then proceed to examine the extent to which the linear response (LR) formulation is applicable. Then, we discuss the generation of holes in the electronic stopping process of ionizing radiation. This hole population analysis is relevant due to the fact that DNA damage derives from subsequent chemical reactions of the resulting excited/ionized DNA. The last section discusses the excited hole populations in terms of both their energetic distributions (i.e., proximity to HOMO, low-lying states, etc.) and their spatial distributions (side chain, nucleobases, proximity to ion track, etc.). The resultant observations have direct implications for the relaxation process of excited holes, which is the next logical step in the first-principles simulation study of DNA ion irradiation, and will be addressed in a future study.

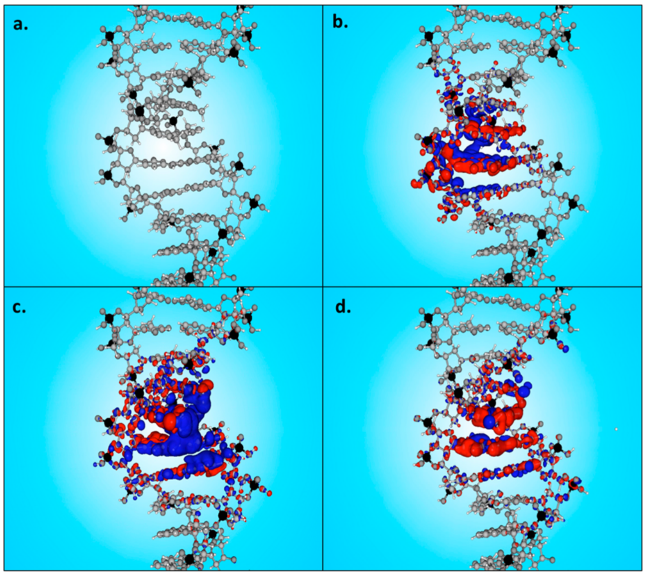

Figure 1. RT-TDDFT simulation snapshots at (a) 0.00, (b) 3.72, (c) 7.44, and (d) 11.16 au in time for a proton traveling at 6.0 au velocity through the center of the DNA molecule. Gray and black spheres show positions of the DNA molecule atoms. Blue (red) isosurfaces indicate increases (decreases) in electron density relative to the ground-state electron density.

3.1. Electronic Stopping Power. In many theoretical studies of electronic responses to ion irradiation, the energy transfer from ion to target electrons is of central importance. The rate of energy transfer, called electronic stopping power, is the key quantity of interest because the velocity dependence of electronic stopping power is what gives rise to the unique energy deposition profile (i.e., Bragg curve) of swift ions. With access to total electronic energy as a function of the swift ion displacement, RT-TDDFT simulations give the quantities necessary for the calculation of this energy-transfer rate. In recent years, significant headway has been made in the use of RT-TDDFT simulations to calculate electronic stopping power for a variety of condensed matter systems ranging from metals,[60−63] semiconductors,[55,64] to liquids.[39]

In order to acquire accurate electronic stopping power curves, it is necessary to take into account the dependence on the projectile ion path in DNA. With this in mind, we have performed an ensemble of trajectories over a range of impact parameters and ion velocities. A total of 16 ion paths through the DNA molecule were simulated, all perpendicular to the periodic direction of the DNA strand, ranging from a path straight through the nucleobase center to a path just outside the sugar-phosphate backbone (see Figure S1 in Supporting Information). Apart from the practical feasibility, this 16-path ensemble allows for direct analysis of the simulations to derive physical insights on effects that are potentially specific to side chain and nucleobase moieties. For each of the 16 paths, 7 ion velocities ranging from 0.25 au to 6.0 au were studied for both protons and α-particles, resulting in a total of 224 RT-TDDFT trajectories. For this 2220-electron system, each of these trajectories comes at a considerable computational cost, illustrating the need in this case for massively parallel implementation.[34,35]

The velocity of the projectile ion is held constant throughout its trajectory. Thus, inherently we have non-equilibrium simulations in which the total energy of the electronic system is not conserved, and work is continuously provided by the projectile ion. This allows us to use the increase in total energy as a quantitative measure of the electronic response to ion irradiation as previously discussed.[34,41] In order to calculate the electronic stopping power from these simulations, we need to calculate the electronic energy change with respect to ion displacement. Unlike in the periodic crystalline system, the electronic energy increases only when the projectile ion penetrates through the DNA. The resulting curve has a sigmoidal form (see Figure S2 in Supporting Information). In this work, we used the approach employed by Sebaugh et al. to define the linear portion of the sigmoid-shaped curves by finding the "bend points".[65] Taking the slope of the linear regression over this region for each RT-TDDFT simulation, we acquire the electronic stopping powers which are then averaged over the ensemble. Figure 2 shows the electronic stopping power as a function of ion velocity for both protons and α-particles with a spline interpolated curve between the simulation data points, and the error bars represent the standard deviation of the mean based on averaging over the 16-path ensemble. The velocities and electronic stopping power at the peaks were determined from this ensemble-averaged curve. These values were compared to the results presented in work by Abril et al.[31] (see Table 1.) in which the electronic stopping power of dry DNA was calculated in the dielectric formalism with energy-loss functions fitted to experimental optical data acquired by Inagaki et al.[44] While there does not exist direct experimental data for the electronic stopping power of these ions in dry DNA, the agreement between our first-principles RT-TDDFT results and the results from the empirically fitted model dielectric function is encouraging for analyzing the details of the simulation in order to derive physical insights. It should also be noted that the calculated electronic stopping power of DNA is quite similar in peak position and overall magnitude to RT-TDDFT-calculated electronic stopping power of liquid water[39] (see Figure S3 in Supporting Information). Because water is the primary component of human tissue, ion beams for cancer therapy are often calibrated with respect to the electronic stopping power of liquid water instead of actual human tissue or DNA.[7] Our results support this practical assumption widely used in radiation oncology.

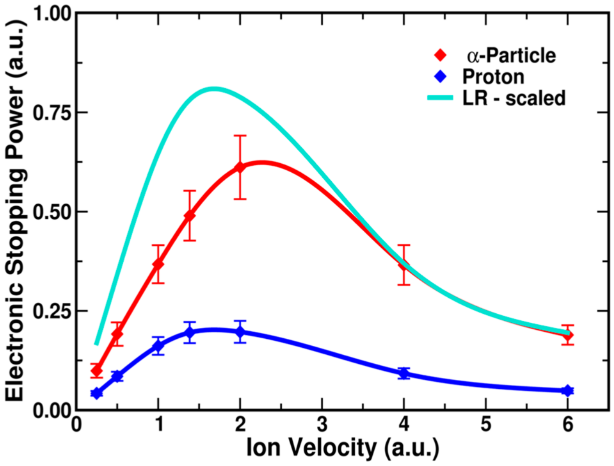

Figure 2. Electronic stopping power averaged over the ensemble of ion trajectories for protons (blue) and α-particles (red) with velocities ranging from 0.25 au to 6.0 au. The LR-scaled electronic stopping power curve (light blue) is acquired by scaling the proton electronic stopping power curve by a factor of 4 (Z^2, where Z = 2).

Table 1. Positions (v_{max}) and Magnitudes (S_{max}) of the Peak Electronic Stopping Power for Protons and α-Particles, in Atomic Units (Hartree/Bohr)[a]

	RT-TDDFT (this work)	Abril et al. 2010	% difference
proton v_{max} (au)	1.64	1.87	−12.2
proton S_{max} (au)	0.202	0.191	+5.76
α-particle V_{max} (au)	2.27	2.22	+2.25
α-particle S_{max} (au)	0.625	0.578	+8.13

[a] Calculated RT-TDDFT results are compared to results by Abril et. al,[29] in which the electronic stopping power of dry DNA was calculated in the dielectric formalism with energy-loss functions fitted to experimental optical data from Inagaki et.[51].

Given its widespread usage in medical physics,[7] it is worthwhile to comment on the extent to which LR theory is valid for the case of DNA. For proton projectiles in crystalline systems, the LR theory model, with the dielectric matrix calculated using linear-response TDDFT, and RT-TDDFT simulations methods show good agreement in calculating the electronic stopping power.[64,66] According to LR theory, electronic stopping power can be expressed in the mathematically closed form:

$$S(v) = \frac{4\pi Z^2}{v^2} L(v) \tag{1}$$

where v is the projectile ion velocity, Z is the atomic number of the projectile ion, and $L(v)$ is a velocity-dependent quantity called the stopping logarithm. There are a variety of ways to represent this stopping logarithm, including the target material's mean excitation energy from Bethe theory[67] and the dielectric function representation in the Lindhard formula.[68] However, the stopping logarithm only depends on the properties of the target material and therefore does not have dependence on the projectile ion species. Instead, the projectile ion species dependence, or Z-dependence, is contained in the Z^2 term, the prefactor in the electronic stopping power formula (eq 1). The resultant electronic stopping power curves incorrectly give the same Bragg peak position for all projectile ion species, unless a separate empirical model for velocity dependent effective charge is employed.[39,62] Additionally, it has been noted that without *ad hoc* extensions to vary Z with respect to velocity, LR theory calculations give inaccurate electronic stopping magnitudes at low ion velocities.[62] According to the LR theory, one would predict for the α-particle case, the stopping power is increased by a factor of 4 ($Z^2 = 2^2$ for α-particle) as shown in Figure 2. In the high-velocity regime, the prediction from the LR scaling agrees well with the RT-TDDFT calculated results. However, the LR-scaled curve and the α-particle RT-TDDFT result begin to diverge toward the Bragg peak, with the LR-scaled curve significantly overestimating the stopping power. The LR-scaled results and the RT-TDDFT results differ by as much as +78% (at $v = 0.5$ au). This significant discrepancy is important especially since the use of heavier ions such as carbon ions has attracted much attention in recent years.[69] These results show that simple scaling of the electronic stopping power for proton by Z^2 would not accurately predict energy deposition when heavier ions are used for irradiation.

3.2. Hole Generation within DNA.

While much discussion in the medical physics field has centered on the energy deposition into electrons as measured by electronic stopping power and how it, assumedly, scales quadratically with the projectile ion charge according to LR theory, such examinations are incomplete for the purpose of characterizing the induced electronic excitations that are responsible for DNA damage. Quantum-mechanical excitations of electrons need to be analyzed not only in terms of energy but also in terms of probability, particularly the quantum-mechanical probability of the hole generation under the ionizing irradiation. The RT-TDDFT quantum dynamics simulations yield probabilistic descriptions of the hole generation as the proton/α-particle penetrates through the DNA.

On the short time span (0.26–6.29 fs, depending on ion velocity) of an individual RT-TDDFT simulation, nuclear motion of atoms in the DNA molecule is negligible, and all target atoms' positions are fixed. Because the DNA molecule remains in its equilibrium geometry, the excitation dynamics can be analyzed by projecting TDKS wave functions onto the KS eigenfunctions of the equilibrium electron density of the neutral DNA system. The excitation dynamics can be then characterized in the framework of single-particle excitations. The hole population change is obtained from calculating the time-dependent occupations of individual KS eigenstates in the valence band as

$$HP(t) = \sum_{j}^{N_{\text{occ}}} \sum_{i} (2 - f_i |\langle \psi_j | \phi_i(t) \rangle|^2) \tag{2}$$

where f_i is the fixed occupation of the TDKS state $\phi_i(t)$, and ψ_j is the KS eigenstates. This same procedure can also be used on the conduction band (CB) states to characterize the excited electrons. Only 3–9% of the excited electrons are recovered when projecting the TDKS onto the set of CB states that covers 6.26 eV above LUMO. The rest is excited into other higher-lying states near/above the vacuum level, which is consistent with the fact that ion beam radiation is indeed ionizing radiation. As expected, the hole population increases as the projectile ion penetrates through the DNA, and it reaches a steady value after the ions leave the DNA (see Figure S4 in Supporting Information). Figure 3 shows the hole population at the end of the simulation (after reaching a steady value) as a function of ion velocity. In the literature, hole generation—or conversely excited electron generation—is often assumed to be directly proportional to electronic stopping power.[70] While this assumption may be valid at high ion velocities, it appears to break down elsewhere in the electronic stopping regime. As can be seen in Figure 3, we observe velocity-dependent hole population trends that are slightly different from those observed in the electronic stopping power curves (Figure 2). Whereas the stopping power peaks at a velocity of approximately $v = 1.68$ au for protons, the hole population has a peak at $v = 0.76$ au. In the case of α-particles, the hole population has a rather flat maximum at $v = 0.87$ au, which is noticeably shifted below the $v = 1.94$ au peak in the stopping power curve.

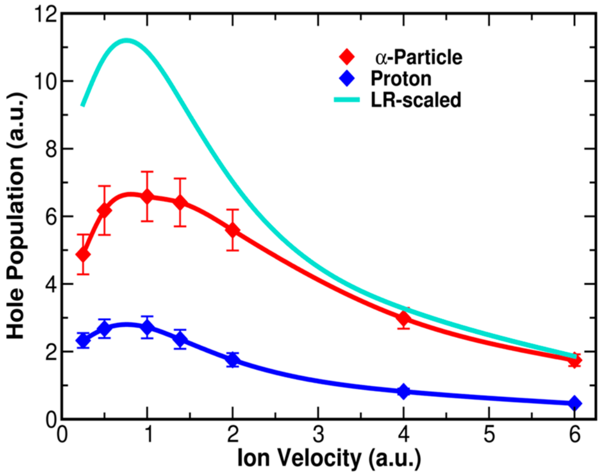

Figure 3. Total hole populations averaged over the ensemble of ion trajectories for protons (blue) and α-particles (red) with velocities ranging from 0.25 au to 6.0 au. The LR-scaled hole population curve (light blue) is acquired by scaling the proton electronic stopping power curve by a factor of 4 ($Z^2 = 2^2$ for α-particles).

Considering the differences between the stopping power curve and hole generation curve peak positions, we note that this could have been expected since the hole population does not take into account the holes' energies. The hole probability distribution with respect to energy eigenstates is broad, as discussed in the next section. Another reason for the difference in the trends is that a significant amount of the electron density is transferred from the DNA to the projectile ions, and not all generated holes are a direct consequence of electronic excitations/ionization *within* the DNA, but instead they are a consequence of charge transfer. We used the Bader charge partitioning scheme[71] implemented in the code by Henkelman et al.[72] to determine the total electronic charge on the proton/α-particle at the end of the simulation, after they excite electrons in the DNA. For the Bader partitioning, charge density isovalues $<10^{-4}$ e$^-$/Å^3 were relegated to vacuum.

Figure 4 shows the projectile ion charge for both proton and α-particle and for two representative paths as a function of the projectile ion velocity. The paths are reflective of two possible types of irradiation-induced excitations: (1) In the "base path" trajectory, the projectile ion passes through the center of the macromolecule, approximately equidistant (~1.7 Å) from the nucleobase pairs above (CG) and below (TA), approximately perpendicular to the hydrogen bonds between the base pairs. (2) In the "side path" trajectory, the projectile ion instead passes close alongside the sugar-phosphate side chain, with a minimum impact parameter of (1.43 Å), which is comparable to the minimum impact of 1.49 Å of the "base path". In both paths, the projectile ion's initial and final positions are over 10 Å away from the nearest atom on the DNA molecule (see Figure S1 in Supporting Information for details). In the high-velocity limit, there is no measurable electron density captured by projectile ions. In the low-velocity regime, however, there is

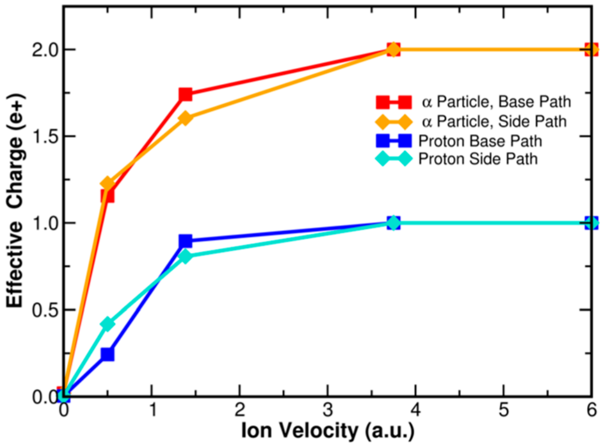

Figure 4. Total hole populations averaged over the ensemble of ion trajectories for protons (blue) and α-particles (red) with velocities ranging from 0.25 au to 6.0 au. The LR-scaled hole population curve (light blue) is acquired by scaling the proton electronic stopping power curve by a factor of 4 ($Z^2 = 2^2$ for α-particles).

appreciable electron density captured by the projectile ions. For protons traveling at a low velocity of 0.5 au, the ion is almost completely neutralized by the electrons stripped from the DNA molecule (~0.8 e$^-$). For α-particles, the amount of charge captured also increases with decreasing ion velocity, but the α-particle has a net ~ +1 charge state at $v = 0.5$ au. For the $v = 0$ au data points, ground-state DFT calculations were carried out with the projectile ions held fixed at fixed positions at the end of the ion track. Similar trends in the velocity-dependent projectile ion charges have been previously observed in silicon carbide[64] and liquid water,[39] with some dependence on the target material. These observations also indicate that the bare-ion assumption employed in LR theory is only valid for high ion velocities beyond the Bragg peak.

Just as we examined the validity of LR theory scaling for predicting electronic stopping power for heavier ions, we can make a similar examination for hole population trends. In addition to the velocity-dependent hole population curves for protons and α-particles, Figure 3 shows the LR-scaled hole population curve, acquired by scaling the proton curve by a factor of 4 ($Z^2 = 2^2$ for α-particles). Examining the plots, one can see that the LR-scaled curve significantly overestimates the hole population for α-particles at ion velocities < ~2 au. Approaching higher velocities, however, the LR-scaled curve converges with that of the α-particle. This is similar to the trends, notably the overestimations, of the LR-scaled electronic stopping power curves. This provides further evidence that non-linear effects, charge-transfer dynamics in particular, become important in the electronic stopping of ions with velocities below the Bragg peak, highlighting the need for high levels of theory and computation for predictions in this regime.

3.3. Energetic and Spatial Distribution of Excited Holes.

3.3.1. Energy Distribution of Excited Holes. The hole populations discussed in the previous section were not decomposed in terms of energy, but such decomposition and analysis in RT-TDDFT simulations is possible and is instructive. If the relaxation of excited holes toward the HOMO is very fast, the energy depth at which the holes are generated has no effect on subsequent chemical reactions of the resulting oxidized DNA. However, very slow relaxation of excited carriers has been observed in some nanomaterials,[73] and future studies are necessary for determining time scales associated with excited hole relaxation in DNA. This time scale is likely to depend significantly on the initial energy of the excited hole generated. Generation of excited holes in deep-lying states with large energy separation would result in a

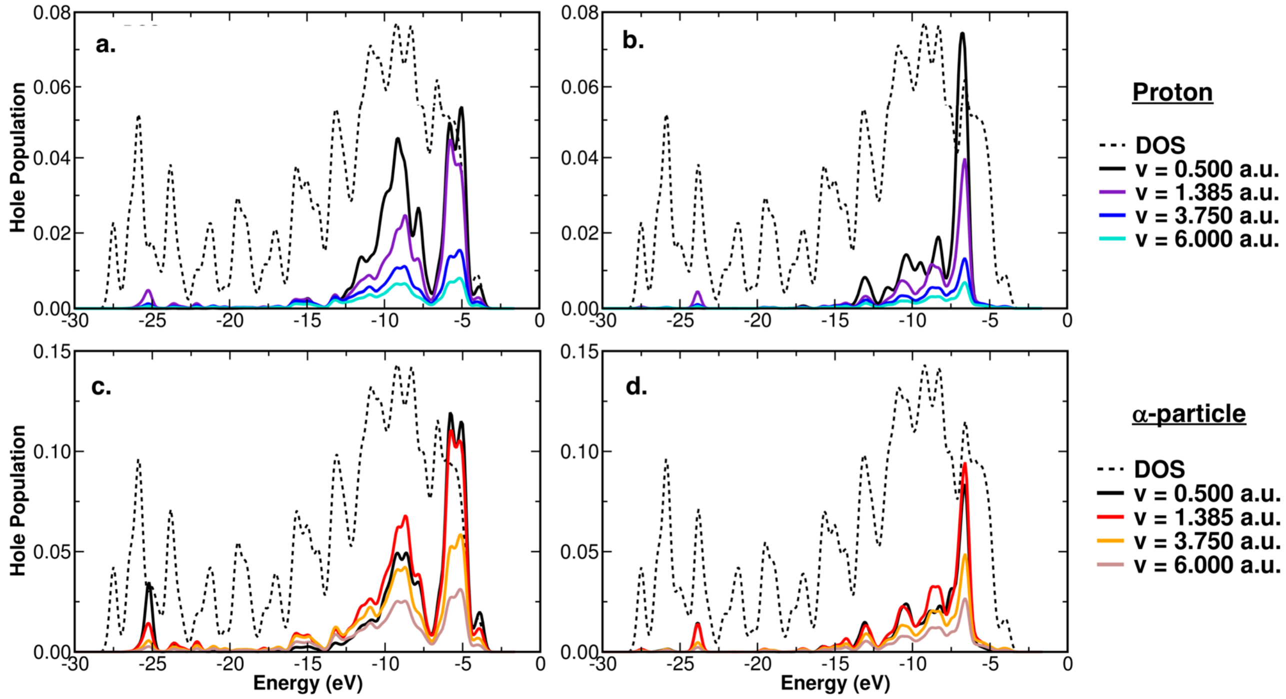

Figure 5. Hole populations plotted as a function of energy based on eigenstate state projections at the end of RT-TDDFT simulations for (a) proton on base path trajectory, (b) proton on side path trajectory, (c) α-particle on base path trajectory, and (d) α-particle on side path trajectory. For reference, the DOS is shown with dashed lines.

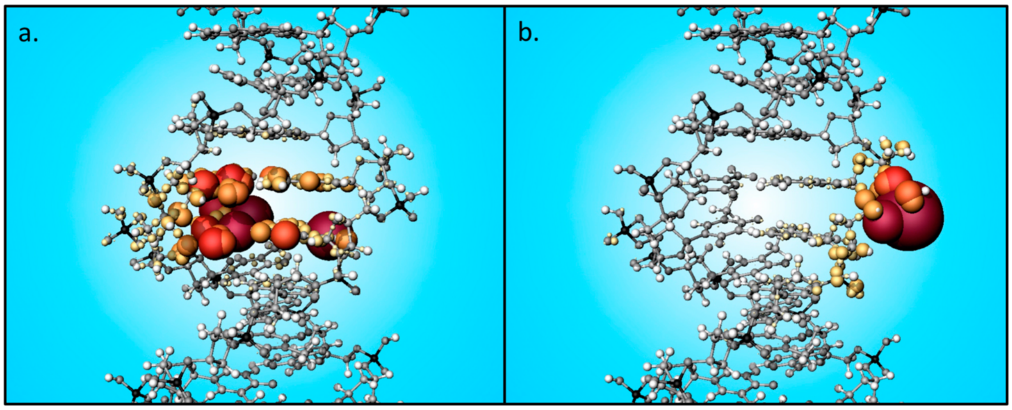

Figure 6. MLWFCs, represented by spheres with color (yellow to dark red) and size proportional to the excited hole population on each center. Smaller, lighter spheres correspond to MLWFs with smaller excited hole populations, and larger, darker red spheres correspond to MLWFs with higher excited hole populations. Atoms in the DNA molecule are shown in greyscale for clarity. (a) Snapshot at the end of RT-TDDFT simulation of proton with $\nu = 1.5$ on the base path trajectory. (b) Snapshot at the end of RT-TDDFT simulation of proton with $\nu = 1.5$ on side path trajectory. The MLFWC projected hole distributions are similar for all ion velocities and for α-particles.

rather slow relaxation process, while excited hole generation in the valence band states is likely to yield a rapid relaxation. In most charge transport studies on DNA bases, the guanine base (G) is found to act as the hole trap, and in fact for the DNA strand simulated in this work, the HOMO is localized on guanine. The electronic states associated with sugar-phosphate side chains are significantly deeper in energy.

Here, we focus on the base and side paths with four different velocities of interest: $\nu = 0.500$ (below the Bragg peak), 1.385 (proton Bragg peak), 1.940 (α-particle Bragg peak), 3.750 (above the Bragg peak), 6.000 au (stopping power follows the LR theory description). In order to characterize the hole generation as a function of its energy, we perform the projection detailed in eq 2, but with the removal of the summation over eigenstates, j. The projection can be acquired for each time step of the RT-TDDFT simulation, but we focus here on the projections at the final step of the TDDFT simulation, after the ion has left the vicinity of the DNA molecule. The resulting hole energy distributions are plotted, with a Gaussian broadening of 0.5 eV, in Figure 5. The density of states (DOS) is also plotted in the same figure for convenience.

Comparing the proton and α-particle cases, the features are quite similar, except for the absolute magnitude, although some slight differences in the relative magnitudes of various peaks can be observed. The base path and side path show some differences for the energetic distribution of the generated holes. For the side path, the holes are largely generated in the electronic states (~2.5 eV below HOMO) associated with phosphate and side chain groups, but there are essentially no holes generated in the higher-lying states (above −5 eV near the HOMO) associated with nucleobases. The base path shows a slightly broader distribution than the side path. In spite of these noticeable differences, in both cases and all for velocities, most of the holes (>95%) are generated within ~10 eV of the HOMO. This aspect of both proton and α-particle irradiation hole generation is distinctly different from X/γ-ray photon irradiation that excites/ionizes localized deep-lying core electrons, which can undergo Auger processes.[74]

3.3.2. Spatial Distribution of Excited Holes. For molecularly heterogeneous systems like DNA, characterizing the spatial extent of excited hole generation can have implications for predicting subsequent damage. This is particularly true if the excited hole relaxation to the HOMO happens on the time scale that is comparable or slower than relevant chemical reaction time scale. In such a situation, the spatial dependence of the hole generation could give some insights into different DNA damages (i.e., nucleobase damage, SSB, DSB, etc.). In order to obtain chemical/spatial details of the ion-induced excitations, we analyze the hole generation in terms of projections onto maximally localized Wannier functions (MLWFs),[75] which are computed using the method developed by Gygi et al.[76] The MLWFs are constructed by applying a unitary transformation to the occupied Kohn−Sham (KS) eigenstates such that resulting MLWFs are maximally localized in space, giving a more chemically intuitive representation of the electronic system. This MLWF transformation yields MLWFs that are localized on bonds and lone pairs in the DNA macromolecule, which are easier to interpret than KS states which can be spatially delocalized. By projecting the TDKS states onto these MLWFs, instantaneous hole populations on specific chemical groups in the macromolecule can be computed at each step in the RT-TDDFT simulation.[40] Each MLWF has an associated geometric center (denoted here as MLWFC), which is defined as the expectation value of the position operator on the MLWF. Each MLWF can be identified with a different chemical moiety of the DNA molecule: sugar, phosphate, nucleobase species, etc. In Figure 6, the time-dependent hole populations are decomposed spatially in terms of MLWFCs which belong to different chemical subgroups of the DNA (i.e., DNA base pairs, sugar-phosphate side chain, etc.). In performing this analysis, we observe that the hole distribution is primarily dependent on the projectile ion path, with the base path resulting in hole generation primarily on the nucleobases (>90% on base pairs, for all velocities and ion species on base path), and the side path resulting in hole generation primarily on the side chain (>90% on side chain for all velocities and ion species on side path); see Figure S7 in Supporting Information for details. Figure 6 illustrates this by displaying the hole distribution in terms of MLWFCs scaled and colored by their respective excited hole populations. In these representative snapshots, the excitation by the projectile ions along the base path leads to hole populations on the DNA base pairs, and hole populations on the side chain for the side path. Further decomposition of hole populations into nucleobase species, sugar groups, and

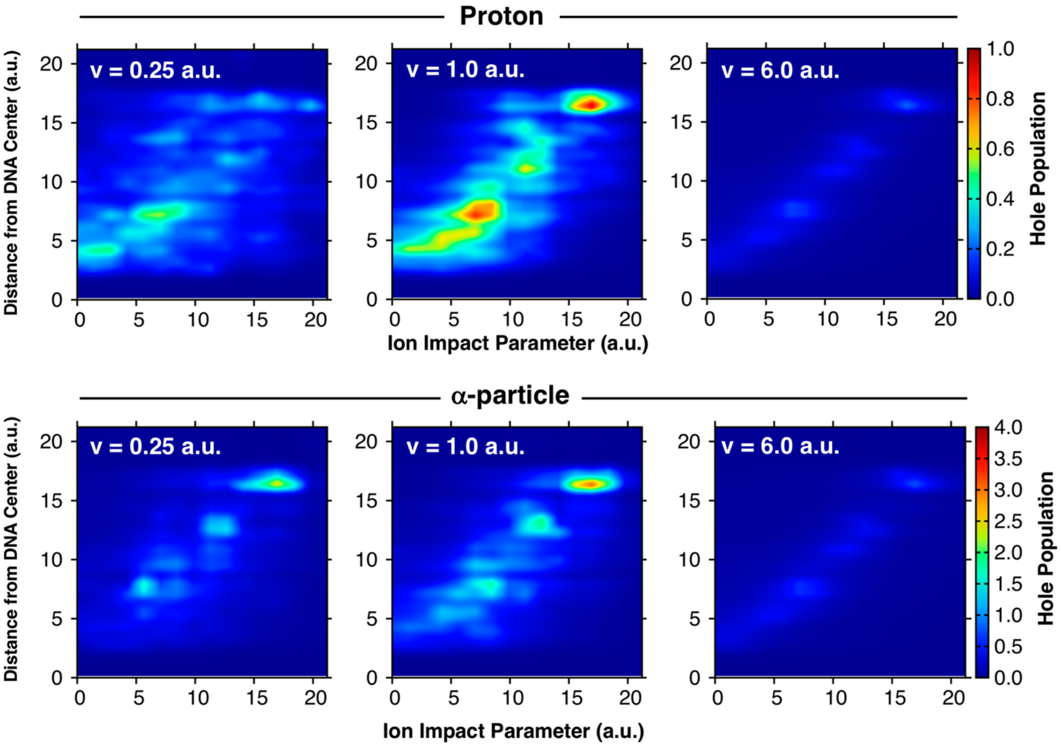

Figure 7. Spatial hole population distributions based on projections onto the ground-state MLWFs for RT-TDDFT simulations of ions impinging on the DNA molecule. The vertical axis indicates the MLWF center displacement from the center (base path) of the DNA molecule, while the horizontal axis indicates the projectile ion impact parameter relative to the center (base path) of the DNA molecule. Results are shown for protons (upper) and α-particles (lower) with velocities of 0.25 au, 1.00 au, and 6.00 au. By plotting displaying the plots in the range from 0.0 to 1.0 (Z^2, where $Z = 1$) for the proton, and in the range from 0.0 to 4.0 (Z^2, where $Z = 2$) for the α-particle, one can directly compare the proton results and the α-particle results to examine the validity of linear-response scaling.

phosphates did not reveal any particular chemical selectivity. In other words, on these time scales, we do not observe specific chemical moieties being more susceptible to the hole generation. Instead, the results suggest that hole generation is a very local phenomenon and is closely tied to proximity of the chemical moieties to the projectile ion trajectory.

In order to further quantify this notion, we return to the ensemble of ion trajectories spanning over a range of impact parameters with respect to the center of the DNA molecule. This 16-trajectory ensemble (see Figure S1 in Supporting Information) shows that hole generations are indeed localized near the path of the projectile ion movement. In Figure 7, the hole distributions are plotted as color maps with respect to two variables: the MLWFC distance from the base path and the impact parameter of the projectile ion relative to the base path. One can observe, by following the diagonal of the maps (Figure 7), that as the ion path is shifted further away from the center of the DNA, the holes distribution follows the same shift away from the center of the DNA. To varying degrees, this trend is evidenced for both protons and α-particles for a range of ion velocities (Figure 7). Approaching lower velocities, the distribution becomes less localized, indicating a larger radial extent of hole generation below the Bragg peak, a result that is consistent with the experimental findings by Souici et al.[26] Importantly, for impact parameters larger than ~18 au (ion trajectory well outside direct impact with the molecule), no appreciable generation of holes is observed. This corroborates the notion that excitations are highly localized around the proton path, ion beams often being described as densely ionizing radiation.[18]

To make comparisons between protons and α-particles, the color maps in Figure 7 are presented in such a way that deviations from LR theory behavior can be identified. The maps in Figure 7, corresponding to the proton-induced hole distributions, have a normalized scale ranging from 0 to 1 (i.e., Z^2, where $Z = 1$), whereas the scale for the α-particle-induced hole distribution maps ranges from 0 to 4, (i.e., Z^2, where $Z = 2$). If the hole generation follows the LR behavior strictly, then the plots in Figure 7 would look identical for protons and α-particles at each velocity. Indeed, for v = 6.00 au, the hole distribution maps look indistinguishable for the proton and α-particle cases, in keeping with the validity of LR theory at high ion velocities. However, for the $v = 0.25$ au and $v = 1.00$ au cases, the hole distribution maps for proton and α-particle differ significantly. For the α-particle cases, the direct correlation between hole distribution and impact parameter is stronger than that observed for the proton, indicating that excitations are more highly localized along the ion path for α-particles than for protons. Thus, it is plausible that the degree of localization is even higher for heavier particles, such as carbon ions. Given this highly localized ionization behavior, it opens up more questions about excited hole localization and delocalization dynamics at longer time scales. We plan to investigate this in a future work.

4. CONCLUSIONS

Electronic excitations are produced when matter is exposed to ion irradiation comprising highly energetic particles such as protons or α-particles. High-energy ion radiation is generally assumed to be ionizing radiation in the same sense as X/γ-rays, which are traditionally more widely used in radiation oncology. However, our work revealed remarkable differences in the typical excitation behavior of proton/α-particle irradiation compared to X/γ-ray photon irradiation. We observe that in the case of ion irradiation, holes are generated mostly in the high-lying valence states near the HOMO, predominantly within the energy range of ~10 eV. We also found that excited hole generation is highly localized spatially along the projectile/ionizing ion track at all proton/α-particle velocities, and its spatial distribution does not show selectivity with regard to the local chemical composition of the DNA (i.e., nucleobase types, side chain, etc.). The electronic excitation effect on DNA quickly decays away from the ion track within a nanometer, as is consistent with the DNA damage behavior found in the experimental work by Souici et al.[24] An intriguing observation in this experimental work was that the maximum DNA damage response was not observed for the proton velocity that yields the highest electronic stopping power, the energy-transfer rate from ions to electronic excitation. Rather, the maximum damage was observed when the proton velocity was higher than the Bragg peak velocity, which corresponds to the maximum electronic stopping power. One might have naively hypothesized that excited hole generation (ionization) is also maximized at this higher proton velocity. However, our first-principles dynamics simulations show that this is not the case. Instead, the hole generation is maximized at velocities that are lower than the Bragg peak velocity for both proton and α-particle.

Our work has revealed, for the first time, that ion beam irradiation results in excited hole generation that is distinctively different from X/γ-rays, and it has also revealed how excited hole generation does not directly correlate with the electronic stopping power trends. Although we have made significant progress in understanding the details of this complex process, further work is needed for building a comprehensive understanding of DNA damage under different types of ionizing irradiation. An important future research direction lies in the investigation of the subsequent relaxation dynamics of the excited holes that are generated under proton and α-particle irradiation. Determining the relaxation time scales of excited holes in DNA represents a key next step in uncovering the highly complex connection between electronic excitations under ionizing radiation and the chemical, bond-breaking mechanisms of DNA damage.

In the context of radiation oncology, the role of solvation, as in biological conditions, needs to be investigated in a future work. One might think that the ionization of DNA is enhanced because electrons can be excited into liquid water. However, our previous works[39,40] have shown that the effective charges of protons/α-particles are significantly reduced in liquid water and that these effective charges have a velocity dependence. Even following from LR theory scaling on the charge, one can reason that the excitations within DNA are significantly suppressed when it is solvated. Given these competing effects, detailed simulations based on first-principles theory will be highly valuable for understanding the role of solvation.

■ ASSOCIATED CONTENT

Ⓢ Supporting Information

The Supporting Information is available free of charge on the ACS Publications website at DOI: 10.1021/jacs.8b12148.

Simulated projectile ion trajectories, total energy and calculating electronic stopping power, electronic stopping power in DNA vs liquid water, total hole populations in RT-TDDFT simulations, charge transfer and its contribution to total hole population, maximally localized Wannier function projected occupations (PDF)

■ AUTHOR INFORMATION

Corresponding Author

*ykanai@unc.edu

ORCID

Dillon C. Yost: 0000-0003-0854-1218

Notes

The authors declare no competing financial interest.

■ ACKNOWLEDGMENTS

This work is supported by the National Science Foundation under grant nos. CHE-1565714, DGE-1144081, and OAC-17402204. An award of computer time was provided by the Innovative and Novel Computational Impact on Theory and Experiment (INCITE) program. This research used resources of the Argonne Leadership Computing Facility, which is a DOE Office of Science User Facility supported under contract DE-AC02-06CH11357.

■ REFERENCES

(1) Verkhovtsev, A.; Surdutovich, E.; Solov'yov, A. V. Multiscale approach predictions for biological outcomes in ion-beam cancer therapy. *Sci. Rep.* **2016**, *6*, 27654.

(2) Donahue, W.; Newhauser, W. D.; Ziegler, J. F. Analytical model for ion stopping power and range in the therapeutic energy interval for beams of hydrogen and heavier ions. *Phys. Med. Biol.* **2016**, *61* (17), 6570.

(3) Surdutovich, E.; Solov'yov, A. V., Multiscale physics of ion-beam cancer therapy. In *Nanoscale insights into ion-beam cancer therapy*, Solov'yov, A. V., Ed. Springer International Publishing: Cham, Switzerland, 2017; pp 1−60.

(4) Durante, M.; Loeffler, J. S. Charged particles in radiation oncology. *Nat. Rev. Clin. Oncol.* **2010**, *7* (1), 37.

(5) Baskar, R.; Lee, K. A.; Yeo, R.; Yeoh, K.-W. Cancer and radiation therapy: current advances and future directions. *Int. J. Med. Sci.* **2012**, *9* (3), 193.

(6) Newhauser, W. D.; Zhang, R. The physics of proton therapy. *Phys. Med. Biol.* **2015**, *60* (8), R155.

(7) Stathakis, S. The physics of radiation therapy. *Med. Phys.* **2010**, *37* (3), 1374−1375.

(8) Paganetti, H., Proton therapy physics. In *Proton therapy physics*, 2nd ed.; Webster, J. G.; Ritenour, E. R.; Tabakov, S.; Ng, K.-H., Eds. CRC Press: Boca Raton, FL, 2018; pp 9−26.

(9) Sevilla, M. D.; Bernhard, W. A., Mechanisms of direct radiation damage to DNA. In *Radiation Chemistry: From Basics to Applications in Material and Life Science*, Spotheim-Maurizot, M.; Mostafavi, M.; Douki, T.; Belloni, J., Eds. EDP Sciences: Les Ulis, France, 2008; pp 191−201.

(10) Uehara, S.; Nikjoo, H.; Goodhead, D. T. Comparison and assessment of electron cross sections for Monte Carlo track structure codes. *Radiat. Res.* **1999**, *152* (2), 202−213.

(11) Wishart, J. F.; Rao, B. M. *Recent trends in radiation chemistry*; World Scientific: Singapore, 2010.

(12) O'Neill, P.; Wardman, P. Radiation chemistry comes before radiation biology. *Int. J. Radiat. Biol.* **2009**, *85* (1), 9−25.

(13) Nguyen, J.; Ma, Y.; Luo, T.; Bristow, R. G.; Jaffray, D. A.; Lu, Q.-B. Direct observation of ultrafast-electron-transfer reactions

unravels high effectiveness of reductive DNA damage. *Proc. Natl. Acad. Sci. U. S. A.* **2011**, *108* (29), 11778−11783.

(14) Baccarelli, I.; Bald, I.; Gianturco, F. A.; Illenberger, E.; Kopyra, J. Electron-induced damage of DNA and its components: Experiments and theoretical models. *Phys. Rep.* **2011**, *508* (1−2), 1−44.

(15) Michael, B. D.; O'neill, P. A sting in the tail of electron tracks. *Science* **2000**, *287* (5458), 1603−1604.

(16) Alizadeh, E.; Orlando, T. M.; Sanche, L. Biomolecular damage induced by ionizing radiation: the direct and indirect effects of low-energy electrons on DNA. *Annu. Rev. Phys. Chem.* **2015**, *66*, 379−398.

(17) Nackerdien, Z.; Olinski, R.; Dizdaroglu, M. DNA base damage in chromatin of γ-irradiated cultured human cells. *Free Radical Res. Commun.* **1992**, *16* (4), 259−273.

(18) Durante, M. In *Biological Effects of Densely Ionizing Radiation*; Proceedings from the World Congress on Medical Physics and Biomedical Engineering, Munich, Germany, September 7−12, 2009; Dössel, O., Schlegel, W. C., Eds.; Springer: New York, 2009; pp 255−257.

(19) Paganetti, H.; Niemierko, A.; Ancukiewicz, M.; Gerweck, L. E.; Goitein, M.; Loeffler, J. S.; Suit, H. D. Relative biological effectiveness (RBE) values for proton beam therapy. *Int. J. Radiat. Oncol., Biol., Phys.* **2002**, *53* (2), 407−421.

(20) Paganetti, H. Relative biological effectiveness (RBE) values for proton beam therapy. Variations as a function of biological endpoint, dose, and linear energy transfer. *Phys. Med. Biol.* **2014**, *59* (22), R419.

(21) Loeffler, J. S.; Durante, M. Charged particle therapy—optimization, challenges and future directions. *Nat. Rev. Clin. Oncol.* **2013**, *10* (7), 411.

(22) Frese, M. C.; Yu, V. K.; Stewart, R. D.; Carlson, D. J. A mechanism-based approach to predict the relative biological effectiveness of protons and carbon ions in radiation therapy. *Int. J. Radiat. Oncol., Biol., Phys.* **2012**, *83* (1), 442−450.

(23) Obolensky, O.; Surdutovich, E.; Pshenichnov, I.; Mishustin, I.; Solov'Yov, A.; Greiner, W. Ion beam cancer therapy: Fundamental aspects of the problem. *Nucl. Instrum. Methods Phys. Res., Sect. B* **2008**, *266* (8), 1623−1628.

(24) Solov'yov, A. V.; Surdutovich, E.; Scifoni, E.; Mishustin, I.; Greiner, W. Physics of ion beam cancer therapy: a multiscale approach. *Phys. Rev. E* **2009**, *79* (1), 011909.

(25) Xu, S.; Guo, D.; Ma, X.; Zhu, X.; Feng, W.; Yan, S.; Zhao, D.; Gao, Y.; Zhang, S.; Ren, X.; et al. Damaging Intermolecular Energy and Proton Transfer Processes in Alpha-Particle-Irradiated Hydrogen-Bonded Systems. *Angew. Chem.* **2018**, *130* (52), 17269−17273.

(26) Souici, M.; Khalil, T. T.; Muller, D.; Raffy, Q.; Barillon, R.; Belafrites, A.; Champion, C.; Fromm, M. Single-and double-strand breaks of dry DNA exposed to protons at Bragg-peak energies. *J. Phys. Chem. B* **2017**, *121* (3), 497−507.

(27) Nováková, E.; Vyšín, L.; Burian, T.; Juha, L.; Davídková, M.; Múčka, V.; Čuba, V.; Grisham, M. E.; Heinbuch, S.; Rocca, J. J. Breaking DNA strands by extreme-ultraviolet laser pulses in vacuum. *Phys. Rev. E* **2015**, *91* (4), 042718.

(28) Zheng, Y.; Wagner, J. R.; Sanche, L. DNA damage induced by low-energy electrons: electron transfer and diffraction. *Phys. Rev. Lett.* **2006**, *96* (20), 208101.

(29) Ziegler, J. F.; Ziegler, M. D.; Biersack, J. P. SRIM-The stopping and range of ions in matter (2010). *Nucl. Instrum. Methods Phys. Res., Sect. B* **2010**, *268* (11−12), 1818−1823.

(30) Ushigome, T.; Shikazono, N.; Fujii, K.; Watanabe, R.; Suzuki, M.; Tsuruoka, C.; Tauchi, H.; Yokoya, A. Yield of single-and double-strand breaks and nucleobase lesions in fully hydrated plasmid DNA films irradiated with high-LET charged particles. *Radiat. Res.* **2012**, *177* (5), 614−627.

(31) Abril, I.; Garcia-Molina, R.; Denton, C. D.; Kyriakou, I.; Emfietzoglou, D. Energy loss of hydrogen-and helium-ion beams in DNA: calculations based on a realistic energy-loss function of the target. *Radiat. Res.* **2011**, *175* (2), 247−255.

(32) Galli, G.; Pasquarello, A. First-principles molecular dynamics. In *Computer simulation in chemical physics*; Allen, M. P., Tildesley, D. J., Eds.; Springer: Dordrecht, 1993; Vol. *397*, pp 261−313.

(33) Strohmaier, E.; Meuer, H. W.; Dongarra, J.; Simon, H. D. The top500 list and progress in high-performance computing. *Computer* **2015**, *48* (11), 42−49.

(34) Schleife, A.; Draeger, E. W.; Anisimov, V. M.; Correa, A. A.; Kanai, Y. Quantum dynamics simulation of electrons in materials on high-performance computers. *Comput. Sci. Eng.* **2014**, *16* (5), 54−60.

(35) Draeger, E. W.; Andrade, X.; Gunnels, J. A.; Bhatele, A.; Schleife, A.; Correa, A. A. Massively parallel first-principles simulation of electron dynamics in materials. *Journal of Parallel and Distributed Computing* **2017**, *106*, 205−214.

(36) Andrade, X.; Strubbe, D.; De Giovannini, U.; Larsen, A. H.; Oliveira, M. J.; Alberdi-Rodriguez, J.; Varas, A.; Theophilou, I.; Helbig, N.; Verstraete, M. J.; et al. Real-space grids and the Octopus code as tools for the development of new simulation approaches for electronic systems. *Phys. Chem. Chem. Phys.* **2015**, *17* (47), 31371−31396.

(37) Pemmaraju, C.; Vila, F.; Kas, J.; Sato, S.; Rehr, J.; Yabana, K.; Prendergast, D. Velocity-gauge real-time TDDFT within a numerical atomic orbital basis set. *Comput. Phys. Commun.* **2018**, *226*, 30−38.

(38) Noda, M.; Sato, S. A.; Hirokawa, Y.; Uemoto, M.; Takeuchi, T.; Yamada, S.; Yamada, A.; Shinohara, Y.; Yamaguchi, M.; Iida, K.; et al. SALMON: Scalable Ab-initio Light-Matter simulator for Optics and Nanoscience. *Comput. Phys. Commun.* **2019**, *235*, 356−365.

(39) Reeves, K. G.; Yao, Y.; Kanai, Y. Electronic stopping power in liquid water for protons and α particles from first principles. *Phys. Rev. B: Condens. Matter Mater. Phys.* **2016**, *94* (4), 041108.

(40) Reeves, K. G.; Kanai, Y. Electronic excitation dynamics in liquid water under proton irradiation. *Sci. Rep.* **2017**, *7*, 40379.

(41) Schleife, A.; Draeger, E. W.; Kanai, Y.; Correa, A. A. Plane-wave pseudopotential implementation of explicit integrators for time-dependent Kohn-Sham equations in large-scale simulations. *J. Chem. Phys.* **2012**, *137* (22), 22A546.

(42) Castro, A.; Marques, M. A.; Alonso, J. A.; Bertsch, G. F.; Rubio, A. Excited states dynamics in time-dependent density functional theory. *Eur. Phys. J. D* **2004**, *28* (2), 211−218.

(43) Gygi, F. Architecture of Qbox: A scalable first-principles molecular dynamics code. *IBM J. Res. Dev.* **2008**, *52*, 137−144.

(44) Inagaki, T.; Hamm, R.; Arakawa, E.; Painter, L. Optical and dielectric properties of DNA in the extreme ultraviolet. *J. Chem. Phys.* **1974**, *61* (10), 4246−4250.

(45) Hamann, D.; Schlüter, M.; Chiang, C. Norm-conserving pseudopotentials. *Phys. Rev. Lett.* **1979**, *43* (20), 1494.

(46) Vanderbilt, D. Optimally smooth norm-conserving pseudopotentials. *Phys. Rev. B: Condens. Matter Mater. Phys.* **1985**, *32* (12), 8412.

(47) Persson, P.; Lunell, S.; Szöke, A.; Ziaja, B.; Hajdu, J. Shake-up and shake-off excitations with associated electron losses in X-ray studies of proteins. *Protein Sci.* **2001**, *10* (12), 2480−2484.

(48) Yao, Y.; Yost, D. C.; Kanai, Y., K-shell Core Electron Excitations in the Electronic Stopping of Protons in Water. **2019**, *arXiv preprint arXiv:1903.03194* (accessed March 8, 2019).

(49) Li, L.; Kanai, Y. Excited Electron Dynamics at Semiconductor-Molecule Type-II Heterojunction Interface: First-Principles Dynamics Simulation. *J. Phys. Chem. Lett.* **2016**, *7* (8), 1495−1500.

(50) Wong, J. C.; Li, L.; Kanai, Y. Size Dependence and Role of Decoherence in Hot Electron Relaxation within Fluorinated Silicon Quantum Dots: A First-Principles Study. *J. Phys. Chem. C* **2018**, *122* (51), 29526−29536.

(51) Perdew, J. P.; Burke, K.; Ernzerhof, M. Generalized gradient approximation made simple. *Phys. Rev. Lett.* **1996**, *77* (18), 3865.

(52) Cohen, A. J.; Mori-Sánchez, P.; Yang, W. Insights into current limitations of density functional theory. *Science* **2008**, *321* (5890), 792−794.

(53) Perdew, J. P.; Ernzerhof, M.; Burke, K. Rationale for mixing exact exchange with density functional approximations. *J. Chem. Phys.* **1996**, *105* (22), 9982−9985.

(54) Iikura, H.; Tsuneda, T.; Yanai, T.; Hirao, K. A long-range correction scheme for generalized-gradient-approximation exchange functionals. *J. Chem. Phys.* **2001**, *115* (8), 3540−3544.

(55) Yost, D. C.; Yao, Y.; Kanai, Y. Examining real-time time-dependent density functional theory non-equilibrium simulations for the calculation of electronic stopping power. *Phys. Rev. B: Condens. Matter Mater. Phys.* **2017**, *96* (11), 115134.

(56) Ullrich, C. A. *Time-dependent density-functional theory: concepts and applications*; Oxford University Press: Oxford, 2012; p 211−331.

(57) Ullrich, C. A.; Burke, K. Excitation energies from time-dependent density-functional theory beyond the adiabatic approximation. *J. Chem. Phys.* **2004**, *121* (1), 28−35.

(58) Ullrich, C. A. Time-dependent density-functional theory beyond the adiabatic approximation: Insights from a two-electron model system. *J. Chem. Phys.* **2006**, *125* (23), 234108.

(59) Fuks, J. I.; Lacombe, L.; Nielsen, S. E.; Maitra, N. T. Exploring non-adiabatic approximations to the exchange-correlation functional of TDDFT. *Phys. Chem. Chem. Phys.* **2018**, *20* (41), 26145−26160.

(60) Schleife, A.; Kanai, Y.; Correa, A. A. Accurate atomistic first-principles calculations of electronic stopping. *Phys. Rev. B: Condens. Matter Mater. Phys.* **2015**, *91* (1), 014306.

(61) Maliyov, I.; Crocombette, J.-P.; Bruneval, F. Electronic stopping power from time-dependent density-functional theory in Gaussian basis. *Eur. Phys. J. B* **2018**, *91* (8), 172.

(62) Correa, A. A. Calculating electronic stopping power in materials from first principles. *Comput. Mater. Sci.* **2018**, *150*, 291−303.

(63) Zeb, M. A.; Kohanoff, J.; Sánchez-Portal, D.; Arnau, A.; Juaristi, J.; Artacho, E. Electronic stopping power in gold: The role of d electrons and the H/He anomaly. *Phys. Rev. Lett.* **2012**, *108* (22), 225504.

(64) Yost, D. C.; Kanai, Y. Electronic stopping for protons and α particles from first-principles electron dynamics: The case of silicon carbide. *Phys. Rev. B: Condens. Matter Mater. Phys.* **2016**, *94* (11), 115107.

(65) Sebaugh, J.; McCray, P. Defining the linear portion of a sigmoid-shaped curve: bend points. *Pharmaceutical Statistics: The Journal of Applied Statistics in the Pharmaceutical Industry* **2003**, *2* (3), 167−174.

(66) Shukri, A. A.; Bruneval, F.; Reining, L. Ab initio electronic stopping power of protons in bulk materials. *Phys. Rev. B: Condens. Matter Mater. Phys.* **2016**, *93* (3), 035128.

(67) Bethe, H. Zur theorie des durchgangs schneller korpuskularstrahlen durch materie. *Ann. Phys.* **1930**, *397* (3), 325−400.

(68) Lindhard, J.; Scharff, M.; Schiott, H. Range concepts and heavy ion ranges. *Dansk, Vidensk. Selsk, Mat-Fys. Medd* **1963**, *33*, 14.

(69) Ebner, D. K.; Kamada, T. The emerging role of carbon-ion radiotherapy. *Front. Oncol.* **2016**, *6*, 140.

(70) Rossi, H. H.; Rosenzweig, W. A device for the measurement of dose as a function of specific ionization. *Radiology* **1955**, *64* (3), 404−411.

(71) Bader, R. F. Atoms in molecules. *Acc. Chem. Res.* **1985**, *18* (1), 9−15.

(72) Henkelman, G.; Arnaldsson, A.; Jónsson, H. A fast and robust algorithm for Bader decomposition of charge density. *Comput. Mater. Sci.* **2006**, *36* (3), 354−360.

(73) Kilina, S. V.; Neukirch, A. J.; Habenicht, B. F.; Kilin, D. S.; Prezhdo, O. V. Quantum zeno effect rationalizes the phonon bottleneck in semiconductor quantum dots. *Phys. Rev. Lett.* **2013**, *110* (18), 180404.

(74) Yokoya, A.; Ito, T. Photon-induced Auger effect in biological systems: A review. *Int. J. Radiat. Biol.* **2017**, *93* (8), 743−756.

(75) Marzari, N.; Vanderbilt, D. Maximally localized generalized Wannier functions for composite energy bands. *Phys. Rev. B: Condens. Matter Mater. Phys.* **1997**, *56* (20), 12847.

(76) Gygi, F.; Fattebert, J.-L.; Schwegler, E. Computation of maximally localized Wannier functions using a simultaneous diagonalization algorithm. *Comput. Phys. Commun.* **2003**, *155* (1), 1−6.